Operando NMR characterization of a metal-air battery using a double-compartment cell design

Magali Gauthier, Minh Hoang Nguyen, Lucie Blondeau, Eddy A Foy, Alan Wong

Operando NMR characterization of a metal-air battery using a double-compartment cell design

Magali Gauthier [**], Minh Hoang Nguyen [1], Lucie Blondeau, Eddy Foy, Alan Wong [*]

Université Paris-Saclay, CEA, CNRS, NIMBE, 91191, Gif-sur-Yvette, France

ABSTRACT

Applying operando investigations is becoming essential for acquiring fundamental insights into the reaction mechanisms and phenomena at stake in batteries currently under development. The capability of a real-time characterization of the charge/discharge electrochemical pathways and the reactivity of the electrolyte is critical to decipher the underlying chemistries and improve the battery performance. Yet, adapting operando techniques for new chemistries such as metal-oxygen (i.e. metal-air) batteries introduces challenges in the cell design due notably to the requirements of an oxygen gas supply at the cathode. Herein a simple operando cell is presented with a two-compartment cylindrical cell design for NMR spectroscopy. The design is discussed and evaluated. Operando ^{7}Li static NMR characterization on a Li–O$_2$ battery was performed as a proof-of-concept. The productions of Li$_2$O$_2$, mossy Li/Li dendrites and other irreversible parasitic lithium compounds were captured in the charge/discharge processes, demonstrating the capability of tracking the evolution of the anodic and cathodic chemistry in metal-oxygen batteries.

1. Introduction

The rechargeable lithium-oxygen (Li–O$_2$) – or lithium-air – battery has recently attracted much attention as a possible high-energy storage alternative to lithium ion battery. Theoretically, it offers a significant high specific energy ~3500 W h kg^{-1} in the discharged state (based on the formation of lithium peroxide Li$_2$O$_2$ as a discharge product from the reaction of Li ions and O$_2$ gas) by combining the light lithium metal and the natural abundance of oxygen supply as the active materials [1–4]. Despite this, the development of Li–O$_2$ batteries is still at its infancy and has not yet attained its full working potential. Fundamental insights on the reaction pathways during charge and discharge are needed to improve Li–O$_2$ batteries' performance further. Various advanced in situ (or operando) characterization techniques have played valuable roles for extracting the real-time chemistries in Li–O$_2$ batteries. For example, in situ microscopy techniques, such as scanning electron microscopy (SEM) [5] or transmission electron microscopy (TEM) [6] have unfolded the morphologies of the discharge products (e.g. Li$_2$O$_2$) and their evolution during cycling; or the use of operando X-ray diffraction (XRD) for identifying in real-time the crystalline Li$_2$O$_2$ product [7]. A comprehensive summary of the in situ and operando characterizations to probe the interfaces of Li–O$_2$ batteries can be found in a recent review [2].

While the studies above have evidenced the main discharge product as Li$_2$O$_2$ in non-carbonated based electrolytes such as glymes, other techniques such as X-Ray Photoelectron spectroscopy (XPS) [8,9] or differential electrochemical mass spectrometry (DEMS) [10–12] demonstrated that parasitic reactions involving electrolyte solutions, Li$_2$O$_2$ and carbon electrodes occur on charge. Notably, DEMS experiments have shown that the amount of O$_2$ released in charge is lower than what is expected from the 2e$^-$/O$_2$ ratio for the decomposition of Li$_2$O$_2$ [10,12,13]. In the case of electrolytes based on 1,2-dimethoxyethane (DME), parasitic reactions are observed even at very low potentials in charge and are responsible for the formation of compounds such as CO$_2$, Li$_2$CO$_3$, lithium-formate and -acetate [8,9,14,15]. While these reactions were first ascribed to the reactivity of electrolyte or carbon with superoxides and peroxides, more recently, the critical role of highly reactive singlet ^{1}O$_2$ has been brought to attention [3,4,10,13,16]. It was found that the singlet ^{1}O$_2$ forms from superoxide and peroxide during discharge, and mostly in the early stages of charge at low potential (< 3.5V). The reactivity of the singlet oxygen with the cell components is

---

responsible for most parasitic reactions in DME-based electrolytes and explains the formation of parasitic products such as Li_2CO_3, Li-formate and -acetate [3,4,10,17].

Ex situ solid-state NMR has been applied to Li–O_2 batteries [18–23]. These studies may not provide a realistic view of the battery reactions and may lead to biased data and misinterpretation, particularly knowing the high reactivity of products formed in Li–O_2 batteries. On the contrary, in situ (or operando) NMR has yet to be exploited for Li–O_2 (or metal-O_2 in general) studies, although NMR characterization can provide complementary information on amorphous products. This is attributed to the challenges of incorporating an O_2 gas electrode in a working NMR cell or probe.

The current operando NMR development has been mostly focused on the cell designs, which must adapt to the NMR requirements (e.g. non-metallic materials, electrode size) and must present specific characteristics for electrochemistry (e.g. hermetical sealing and good mechanical pressure on the stack). Few designs – such as plastic flat bag, plastic cylindrical Swagelok and plastic capsule – have found successes in Li-ion batteries [24,25]. It is also worth mentioning that a clever NMR cell design based on a plastic jelly-roll cell was recently introduced [26], allowing for the first time in situ MAS experiments (i.e. stop-and-MAS) to be carried out without dismantling the cell. Despite the advancements, these cell designs mostly apply to metal or metal-ion chemistries based on intercalation or insertion and do not allow to monitor more complex battery chemistries. Indeed, performing operando NMR on metal-oxygen batteries brings additional challenges with the need for oxygen in the cell. There are two options that can be considered: (1) an open-gas system which allows a continuous flow of gas to the porous cathode; or (2) a close system with a gas reservoir directly connected to the porous cathode. A recent design of an open system was patented but has yet been fully explored [27]. Herein, we introduce a close system design with a double-compartment cylindrical cell, where one cylinder operates as a gas reservoir and the other hosts the electrodes stack. The advantages of a close-gas design are the easy handling of the operando experiments, without the need to connect to a gas supply, and eliminate the possibility of electrolyte evaporation through gas flow. The drawback is the limited gas supply for the redox reactions. As a proof of concept study, two complete charge/discharge cycles of a Li–O_2 cell were analyzed with operando ^{7}Li NMR.

2. Materials and methods

2.1. Description of the electrochemical NMR cell

The general criteria of an electrochemical NMR cell for operando (and in situ) measurements are as the following: (i) be built from non-metallic materials to eliminate interference with the strong magnetic field; (ii) provide robust airtightness and cell compression for cyclability and durability; (iii) allow for sufficient electrode mass loading for detection sensitivity, and lastly (iv) the cell geometry must take into account the space available inside the probehead. In addition to these criteria, the cell introduced herein is also complicated by the oxygen gas electrode. As shown in Fig. 1, we address this by a design of two-joined cylinders. The top large cylinder consists of a gas chamber (with a 655 mm^3) and a long 9 mm screw cap connected to a smaller cylinder hosting the electrodes. The benefit of the two compartments design is that it allows a larger volume for the O_2 storage to give sufficient O_2 for the redox reactions, while the smaller compartment provides greater B_1 efficiency from the rf coil. Moreover, it ensures a good pressure on the cell stack through the junction of the two compartments, as no suitable spring can be used inside the NMR magnet. A series of gas passages (with a diameter of 0.5 mm) are integrated into the connecting screw cap allowing the gas passage from the gas chamber to the electrodes. The gas chamber is sealed with a top cap consisting of 1.2 mm diameter inlet- and outlet-gas silicone tubings, which are regulated by Omni fit® connectors. For a close-gas system used in this study, these connectors are closed after the gas injection. However, the design could readily adopt an open system by directly connecting a gas source through the inlet tubing during the operando measurements. The remote distance from the electrode should prevent electrolyte evaporation by the gas flow. Lastly, the double-compartment design could, in principle, allow for an independent large volume rf coil around the gas chamber for monitoring the gas content with an individual circuit.

Circular electrodes are hosted at the smaller cylinder center with a stacking arrangement from top to bottom: cathode/separator/anode. Substantially, the cathode (i.e. gas electrode) is in direct contact with the above gas chamber through the gas passages. The electrodes are compressed by the torque tension generated by two long screw caps, each with a length of 9 mm and with a pitch thread of 1 mm. A 0.8 mm Cu-wire – as a current collector – is inserted at both ends of the cell contacting the anode and cathode. The entire cell body is made of polyether ether ketone (PEEK), which has the essential properties for an NMR battery cell:

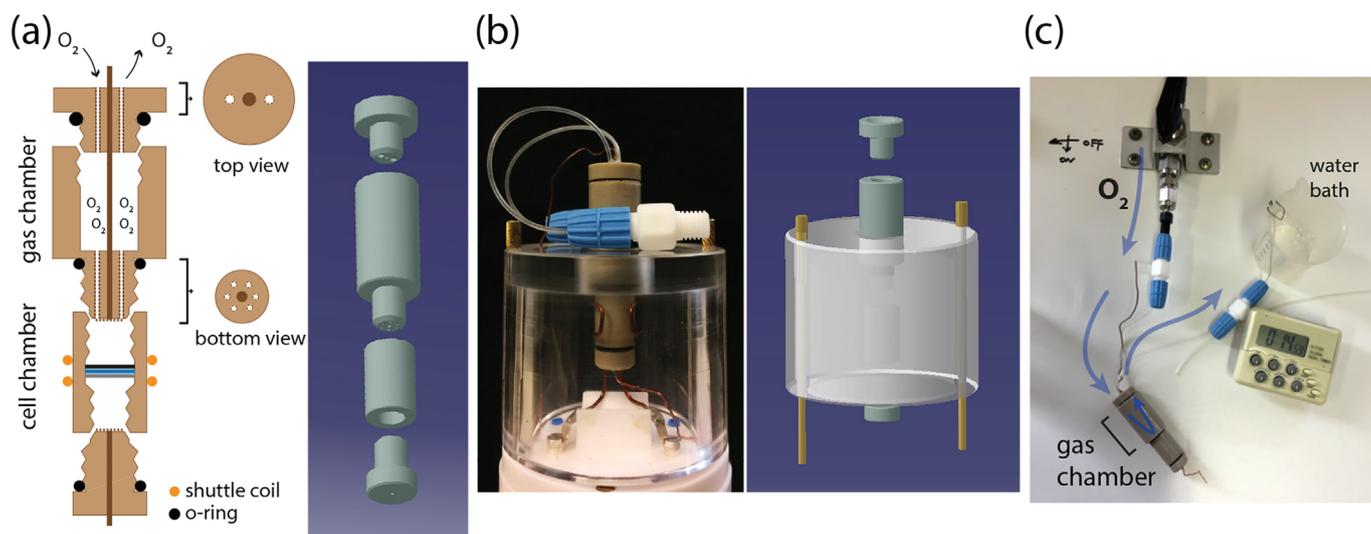
Fig. 1. Design of a M − O_2 cell for operando NMR experiment. (a) Schematic drawing and model of the double-compartment cylindrical cell, showing the two joint cylinders acting as a chamber for either the gas or the electrodes. (b) Photograph and model of the cell mounted on the NMR probehead. The cell is under a close-gas setup. (c) Gas-filling station showing the direction of the gas flow.

rigid non-conductive material, resistant to mechanical stress [28] and chemically inert to metallic lithium and conventional electrolytes used in batteries [25]. Nitrile O-rings ensure hermetic sealing of the cell at all interlocking.

2.2. Experimental procedure

2.2.1. Operando NMR

^{7}Li NMR was carried out on a Bruker Avance II spectrometer operating at a frequency of 194.02 MHz with an 11.75 T NMR magnet with a single channel automatic tuning matching (ATM) NMR probe (NMR Service GmbH). The probe allows a rapid automated frequency tuning before each sequential spectral acquisition during the operando measurements. The probe also accommodates the connections for galvanostatic measurements with the potentiostat. A detail description of the ATM and its experimental setup can be found in Ref. [29].

The probehead was modified with a cylindrical Plexiglas holder supporting the double-compartment cylindrical cell at an upright position (Fig. 1 b). This permits using a saddle coil wrapped closely around the center of the small cylinder containing the electrodes for an optimal sensitivity (maximum filling factor) in the data acquisition. The coil offers a 50% B_1 homogeneity for the entire detection volume (~900 mm^3); a higher % is expected for the electrode cell (< 115 mm^3) centered at the coil.

Operando spectra were collected by a series of 32 sequential single-pulse experiments during the 64 h potential cycling using a single $\pi/4$ pulse (4.5 μs), each with a 5 s recycle delay, 200 kHz sweep width, and a 1400 scan. Each individual operando spectrum was processed and phased individually in the Bruker Topspin software. The chemical shift was referenced to an external 1 M LiCl at 0 ppm.

The line fittings were carried out with the DMFit program [30] using a Gaussian/Lorentzian line shape function. The error bars were deduced by propagating the errors reported for the fitted line width and amplitude. Data processing was done in Excel. Note that the operando NMR measurements were repeated twice with the same Li–O₂ electrode components using the double-compartment cell. The similar spectral results illustrate the potential of data reproducibility (Fig. S1).

2.2.2. Li–O₂ cell assembly and electrochemistry

The positive electrodes were prepared using either high surface area Carbon black or Carbon Nanotubes (CNTs). Carbon black electrodes were prepared by mixing Carbon Black Super P (99 þ %, Alfa Aesar) with poly(tetrafluoroethylene) binder (PTFE, 60% wt. dispersion in H₂O, Sigma Aldrich) in a 9:1 ratio with isopropanol. The slurry obtained was then deposited on a 6 mm diameter copper mesh (80 mesh). For the CNTs cathodes, nanotubes produced by Chemical Vapor Deposition were directly deposited on a copper mesh (6 mm in diameter). For both carbon black and CNT cathodes, the density of carbon was around 1 mg cm^{-2}. In each case, the electrodes were dried in vacuum for 24 h at 100 °C. Cell assembly was entirely conducted in an Ar-filled glovebox by stacking inside the cell chamber the cathode, two glass micro fiber separators (Whatman GF/A) soaked with electrolyte and a 6 mm disk of lithium metal (99.9%) as the negative electrode. The electrolyte used was 1 M lithium bis(trifluoromethanesulfonyl)imide (LiTFSI, 99.9%, Sigma Aldrich) in 1,2-dimethoxyethane (DME, 99.5%, Acros Organics). Prior to electrolyte's preparation, the LiTFSI lithium salt was dried in vacuum for 24 h at 100 °C.

After assembly in the glovebox, the Li–O₂ cells were transported to a gas filling station (Fig. 1 c), and purged with pure O₂ at 0.5 bar for ca. 15 min using Omni fit® connectors. After closing the gas-outlet, the inlet was maintained open for 30 s to build up a positive pressure inside the cell.

Galvanostatic measurements were performed at room temperature using a research-grade potentiostat (Biologic, SP50). The current density was 100 mA g$_{carbon}^{-1}$ (g$_c^{-1}$) of carbon (~0.1 mA cm^{-2}) with a potential range of 2.0–4.0 V$_{Li}$. In some cases, the capacity was fixed to 500 or 1000 mAh g$_c^{-1}$.

2.2.3. Ex situ characterization

XRD and SEM characterizations were performed on discharged electrodes after disassembling the cell. A RU-200B rotating anode X-ray generator using monochromatized Mo radiation (λ ¼ 0.7093 Å) was used for XRD measurements. Spherical diffraction patterns were acquired using a photo-sensitive plate that was digitized using a scanner. We used the FIT2D [31] software to integrate the diffraction patterns. We collected the SEM images using a SEM-FEG Zeiss Ultra 55 model operating at 3 kV. To avoid reactivity with air before-and-during the XRD measurement, samples were protected with Kapton tape in the glovebox before the measurement. For SEM, electrodes were stored in argon before being quickly placed (< 30 s) into the microscope to minimize as much as possible air exposure.

3. Results and discussion

3.1. Cycling performance of the NMR cell for Li–O₂ chemistry

Before performing operando measurements on a Li–O₂ system, we first verified the reliability of the Li–O₂ cell chemistry outside the NMR probe in the dedicated cell, which means evaluating the cycling performance and the cell's ability to support Li–O₂ discharge and charge. In particular, we examined the oxygen reduction reaction (ORR) and oxygen evolution reaction (OER) on a carbon nanotubes (CNTs) electrode through galvanostatic cycling. Fig. 2 a shows the potential profile as a function of capacity (per carbon weight) at a current rate of 100 mA g$_c^{-1}$ with a capacity fixed at 1000 mAh g$_c^{-1}$ in a 1 M lithium bis(trifluoromethanesulfonyl) imide (LiTFSI) in 1,2-dimethoxyethane (DME) electrolyte. To evaluate the cell's reproducibility, a similar measurement on carbon black electrode was performed (Fig. S2) with a capacity limited at 500 mAh g$_c^{-1}$. A single plateau is observed around 2.5–2.6 V$_{Li}$ in discharge for both CNTs (Fig. 2 a) and carbon black electrodes (Fig. S2b), in good agreement with literature [32–37]. The electrochemical signature of the cell points thus toward the formation of the expected discharge product Li₂O₂ following the reaction:

$$2Li^{þ} þ 2e^{-} þ O_2 \quad Li_2O_2$$
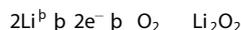
The polarization is modest regarding to the thermodynamic potential for the formation of Li₂O₂ (E$_{Li2O2}$ ¼ 2.96 V$_{Li}$ [1]). The overpotential is also low in charge, with a charge plateau and the end of charge potential around 3.7–3.8 V$_{Li}$. This is promising as carbon-based electrodes have usually charging potentials above 4 V$_{Li}$ [34,38], but in line with the end of charge potentials reported in the literature for CNT-based electrodes (between 3.3 and 4.0 V) [35–37]. While the electrochemistry results hint at the formation and decomposition of Li₂O₂ during discharge/charge processes, it is yet important to keep in mind that the galvanostatic cycling reflects only the evolution of the potential and the current generated, whether or not the latter results from wanted or unwanted electrochemical processes such as the degradation of the electrolyte or the electrode [13].

In terms of cycling stability, charge and discharge plateaus are maintained for a dozen of cycles at a capacity of 500 mAh g$_c^{-1}$ for carbon black electrodes (Fig. S2b) and at least 4 cycles for the CNTs electrodes at a capacity of 1000 mAh g$_c^{-1}$ (Fig. 2 a). The cyclability is modest as expected for Li–O₂ cells. Globally, the NMR dedicated cell cycling is comparable for the first few cycles to literature and is thus suitable for operando measurements [3,4,36,37]. Fig. 2 b shows the ex situ XRD pattern of a CNT cathode at the end of the first discharge. The dominant peak situated at around 12 ° refers to the pristine CNT substrate (Fig. S3). Three other peaks located at 15.0, 16.0 and 18.5 ° (2θ) correspond to the crystalline Li₂O₂ phase, which is the expected discharge product. These XRD results consequently verified that the ideal Li–O₂ electrochemistry is taking place inside our NMR dedicated cell. The morphology of Li₂O₂ formed during discharge is highly dependent on the electrode materials and electrolyte, both influencing the reaction pathway, from a surface
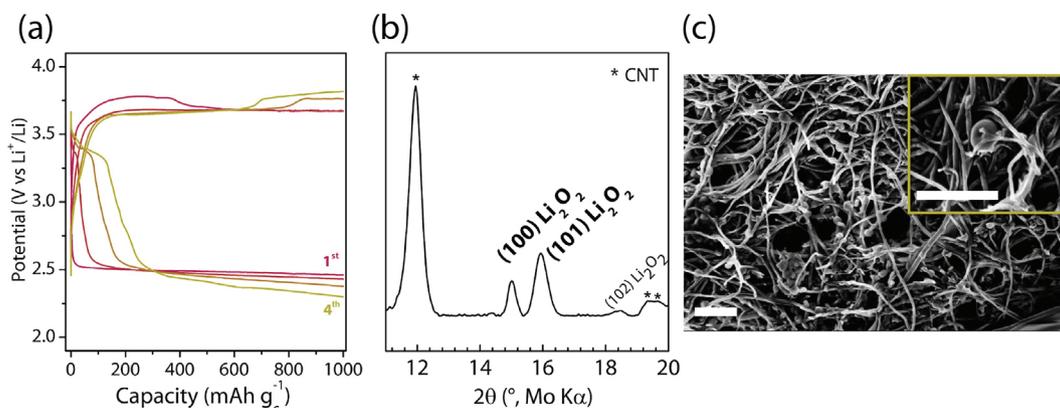
Fig. 2. (a) Galvanostatic Li–O$_2$ discharge-charge cycles at 100 mA g$_c^{-1}$ with a capacity limited at 1000 mAh g$_c^{-1}$ in the NMR cell with a CNTs electrode in 1 M LiTFSI in DME. (b) XRD pattern of a CNTs electrode after one discharge at 100 mA g$_c^{-1}$ with a capacity limited at 1000 mAh g$_c^{-1}$. The peaks are indexed with the 04-013-3506 ICDD card. (c) SEM image of a CNT electrode discharged up to 1000 mAh g$_c^{-1}$ at 100 mA g$_c^{-1}$ in 1 M LiTFSI in DME. Scale bar 1 μm.

dictated reaction to a solution route [2–4]. Thus, SEM analysis was performed at the end of the first discharge on both CNT and carbon black electrodes as a complementary analysis to XRD to confirm further the presence of Li$_2$O$_2$. Li$_2$O$_2$ is evidenced in both electrodes in the form of toroids, which grow around the carbon nanotubes in CNT electrodes (Fig. 2c) or deposit on the carbon surface in carbon black electrodes (Fig. S2c). The toroid is a characteristic shape of Li$_2$O$_2$ crystal formation from the disproportionation of LiO$_2$ intermediates formed in the solution route [33,39]. Assuredly, the above ex situ results from XRD and SEM have affirmed the double-compartment cylindrical cell's reliability for generating the ideal Li–O$_2$ electrochemistry.

3.2. Operando ^{7}Li NMR on a Li–O$_2$ cell

A close-gas system of a Li–O$_2$ cell with a CNTs cathode in a LiTFSI/DME electrolyte was characterized by operando ^{7}Li NMR. The spectral profile obtained at t ¼ 2 h reveals two main resonances (Fig. 3a), a sharp peak at 2.5 ppm associated to the fast mobile Li^þ in the liquid electrolyte (LiTFSI in DME) and a broad resonance at around 250 ppm related to the Li metal anode, which can be deconvoluted into two peaks at 250 ppm for pristine Li metal and 260 ppm for Li mossy-structures deposited on the

bulk metal surface [40]. As expected at the beginning of cycling, no Li dendrites are observed at around 270 ppm. Here, it should be emphasized that the observed NMR intensity corresponds solely to the microstructures at the metal's surface rather than in its total mass. This is ascribed to the skin effect when a radio frequency (rf) is applied. As such, the measured intensity corresponds only to Li within the skin depth (d) layer, which can be formulated by Ref. [41]: d ¼ $\sqrt{\rho / \eth \pi \mu_0 \mu_r \omega_{rf} Þ}$ where ρ ¼ 92.8 n Ω m is the resistivity of Li metal, μ$_0$ ¼ 4π × 10^{-7} m kg A^{-2} s^{-2} is the permeability of the vacuum, μ$_r$ ¼ 1.00002 is the relative permeability of Li metal. In this study at ω$_{rf}$ ¼ 2π 193.8 MHz, the skin depth layer is calculated to be 11 μm.

The spectral profile at t ¼ 40 h after completing a full cycle has changed noticeability (Fig. 3a), indicating the occurrence of electrochemical processes in the Li–O$_2$ cell. The spectrum can now be deconvoluted with five different peaks. In particular, a broad resonance centered at 4 ppm is apparent and indicates the presence of slow mobile diamagnetic Li^þ ions. We suspect these species to be the solid products from (electro)chemistry reactions such as Li$_2$O$_2$ and other parasitic inorganic and organic compounds [19,42]. A detail deduction can be found in Fig. S4 and will be further discussed. Exploiting these resolved Li and Li^þ contributions in the spectra, the operando NMR data set (n ¼ 29
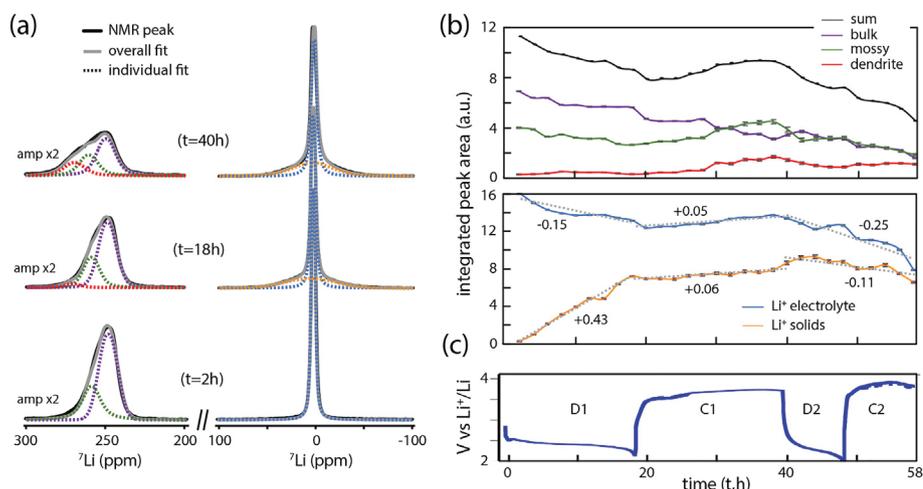

Fig. 3. Operando ^{7}Li NMR spectral results obtained from a close-gas system of a Li–O$_2$ cell with a CNT electrode in a 1 M LiTFSI in DME electrolyte. (a) NMR line-fitting of the operando spectra at t ¼ 2 (beginning of discharge), 18 (end of the first discharge) and 40 h (end of first charge) reveals the spectral evolution at the different cycling periods. Five fitted Gaussian/Lorentzian lines are assigned to pristine Li-metal (purple line at 249 ppm), mossy (green line at 259 ppm) and -dendritic (red line at 271 ppm) structures, as well as a Li^þ electrolyte (blue line at 2.5 ppm) and solids (a broad orange line at 4 ppm). A more in-depth deconvolution of the broad component at 4 ppm can be found in Fig. S4. (b) Time-dependence of the integrated peak areas plotted as a function of the cycling period. The error bars, derived by DMFit [30], indicate the misfit. The mean errors across the cycling are 1.4% for Li-bulk, 2.7% for Li-mossy, 7.0% for Li-dendrite, 0.3% for Li^þ electrolyte and 2.0% for Li^þ solids. In the plot of Li^þ electrolyte and solids lines, the inserted numbers represent the slopes of the tangent lines (dotted grey). (c) The galvanostatic cycling was performed at 100 mA g$_c^{-1}$ during the operando measurement. D1/C1 and D2/C2 correspond to the discharge and charge of the first and second cycle, respectively.

spectra) was fitted with five individual Gaussian/Lorentzian (G/L) lines. The fitting was carried out by constraining the chemical shifts for the pristine Li metal and its microstructures (249, 259 and 271 ppm) and allowing an auto-iteration to fit with the line widths and amplitudes of all five resonances, along with the chemical shifts of the two diamagnetic Li^b peaks (~2.5 and ~4 ppm). Examples of the fits are shown in Fig. 3 a. Each resonance's integrated area was plotted as function of cycling in Fig. 3 b, offering time-resolved quantitative information on the different lithium components in the Li−O_2 cell. The errors were deduced based on the propagation of errors found in the fitted line width and amplitude (reported by DM fit), which are proportional to the area of a G/L line. Overall the errors are small and consistent throughout the operando data indicating a reliable fitting protocol. Larger errors are found mostly for the mossy and dendrite peaks (with a mean of 2.7% and 7.0%, respectively). This reflects the difficulty of fitting the extensive overlapping signals. It should be noted that the use of a short recycle delay (5 s) in the data acquisitions may hindered the spectral interpretation since different T_1 relaxations (long and short) are expected for the different Li^b species formed during the electrochemistry reactions, which would contribute to the broad signal at 4 ppm and the sharp electrolyte peak at 2.5 ppm.

Regardless, the time-dependence peak area of the different Li/Li^b contributions show discrete trends during the difference cycling processes (Fig. 3 b). Herein, we will discuss chronologically in detail the operando data following the electrochemical discharge-charge processes.

During the first discharge (D1), we observed a depletion of the Li metal anode (Fig. 3 b). This reflects as expected the Li stripping from the anode (Li → Li^b + e⁻). On the contrary, a sudden appearance of a broad resonance at 4 ppm is observed during the discharge process and followed by a gradual rise with a positive linear slope (ΔS ¼ þ 0.43), suggesting a rapid formation of discharge solids containing Li^b (Fig. 3 b). Based on the ex situ XRD and SEM results (Fig. 2) and on the theoretical reaction of Li^b and O_2 to form Li_2O_2 (2Li^b þ 2e⁻ þ O_2 → Li_2O_2), the discharge products could include the relevant Li_2O_2 product together with other Li^b species. Unfortunately, the small shift range for the diamagnetic Li^b species (< 10 ppm) hinders the identification of the different compounds. However, one could take advantage of the quadrupolar ^7Li by examining the satellite transition signals to distinguish the Li^b contributions from those with symmetrical environments. A previous ex situ NMR study [19] has shown a very distinct ^7Li static spectral profile between Li_2O_2 and Li_2CO_3: a pair of satellite transition signals are apparent for Li_2CO_3 but absent for Li_2O_2. This suggests a considerable quadrupolar interaction for the former. On this basis, Fig. S4a shows no apparent (or very small) satellite signals at the end of D1 (t ¼ 18 h) which could therefore inexplicitly indicates the sole presence of Li_2O_2 at the end of the first discharge. However, one should consider that other Li^b species with insignificant ^7Li quadrupolar interaction could also contribute to the overall broad signal at 4 ppm. Apart from the possible formation of Li_2O_2 in D1, we interestingly observe a decrease in Li^b of the liquid electrolyte (Fig. 3 b, negative ΔS of −0.15), implying an electrolyte's consumption through decomposition reactions in discharge. The observed non-linearity may indicate the occurrence of multiple processes, which is in line with the previous studies on DME-based electrolytes that demonstrated that the singlet oxygen and Li_2O_2 produced in discharge could react with the glyme electrolyte to produce compounds such as Li_2CO_3, Li-acetate and -formate [10,14]. These compounds can also account for the growth of the broad signal at 4 ppm during D1, but we suspect the extents should be small since no apparent satellite signals are observed (Fig. S4, t ¼ 18 h) as their quadrupolar interactions are expected to be significant to the line shape [19,42,43].

Unlike D1, the first charge (C1) is marked by a sudden growth of the total Li metal signal (Fig. 3 b), corresponding to the predicted reverse reaction of Li plating during charge. The Li metal is mostly deposited in the form of mossy Li or Li dendrites (Fig. 3 b). Singularly, the initial amount of Li that was present before cycling is not fully recovered, suggesting that not all the lithium that was exchanged for the formation of Li_2O_2 in discharge is reversibly going back in charge to the anode. This

indirectly indicates that the oxidation of Li_2O_2 to Li^b and O_2 is not complete and that some Li is consumed in parasitic processes. The same conclusion can be drawn from the evolution of the solid phases resonance during C1 (Fig. 3 b). If the discharge product Li_2O_2 was fully oxidized back to O_2 in charge, we should expect a decrease of the broad resonance at 4 ppm. Instead, a stable evolution is noticed throughout C1, suggesting irreversible products also formed, countering the decrease of signal related to the reversible Li_2O_2 product. These irreversible products could ascribed from the decomposition of electrolyte, discharge products or carbon electrode, and their signals have offset the decreasing of Li_2O_2. Noticeably, the low charging voltage of around 3.8V for the first charge hints at the release of singlet oxygen from Li_2O_2 or LiO_2 reaction pathways [10]. The reactivity of singlet oxygen $^1O_2$ with the cell components such as the electrolyte solvent leads to Li formate, Li acetate and Li_2CO_3 [3,4,10,17], that can here account for the behavior of the broad signal at 4 ppm. As shown in Fig. S4b, this broad signal at t ¼ 40 h (end of C1) can be deconvoluted with two individual lines, one with a pair of quadrupolar satellite line (C_Q ¼ 70 kHz, η_Q ¼ 0.7) and the other with a single G/L. The former could be ascribed to Li^b-organic solids [43,44] and Li_2CO_3 [19], and the latter to Li_2O_2 [19] along with other Li^b species with insignificant C_Q. To avoid confusion, as illustrated in Fig. S4, the single fitted G/L line at 4 ppm shown in Fig. 3 and its discussion is ascribed to all Li^b solid products present in the reactions.

Apart from reactions products from the cathode, note also that the broad signal at 4 ppm may also derived from anode degradation products formed on the Li metal surface. While the XRD and SEM data could not identify these unwanted irreversible products, the operando NMR highlights some components some decomposition and the non-reversibility of the redox reaction in the Li−O_2 cell in DME electrolyte. Based on the weak reversibility of the Li plating on the anode, we can infer that the degradation products are formed in a quite large amount.

Finally, during the second cycle, as expected from Li metal stripping, the intensity of the metal is depleting in D2 (Fig. 3 b). Yet only a small increase of the resonance related to solid Li^b-based products occurs, suggesting a deficient production of Li_2O_2 from the reduction of O_2. It is noteworthy that a rapid degradation of the cell performance begins in C2, indicated by a long flat plateau in charge with a capacity exceeding the one obtained from discharge (Fig. 3 c). During D2 and C2, the liquid electrolyte resonance decreases significantly, while its linewidth increased by ca. 250 Hz (Fig. S5), implying again the presence of electrolyte decomposition and unwanted parasitic reactions. In fact, the second cycle of the operando measurement is highly dominated by these decompositions which is similar to what was observed in the literature [14]. This underlines the poor reversibility of the Li−O_2 cell in these electrolyte solutions.

More supporting characterizations (e.g. ex situ ^7Li, ^{17}O, ^{13}C MAS) are needed to unambiguously elucidate the nature of the degradation products formed here. Regardless, this study exemplifies the discrepancy between the coulometric measurements, suggesting the reversible formation of Li_2O_2, and advanced operando NMR measurements that show here extended degradation of the cell reversibility and formation of parasitic products. This reflects the benefits of using operando techniques to capture the parasitic reactions in real-time and ultimately decipher the complex electrochemical reactions inside operating Li−O_2 batteries.

4. Conclusions

As a proof of concept, this work successfully establishes an operando static ^7Li NMR investigation of the discharge-charge of a Li−O_2 battery. By specifically designing a dedicated cell (double-compartment cylindrical cell) with an oxygen gas reservoir, cycling of a Li−O_2 cell is possible inside the NMR magnet during spectra acquisition. The operando results have unveiled the evolution of the lithium anode microstructures, the growth of discharge products on the cathode, and an extensive amount of degradation products. In agreement with previous investigations performed in the literature, these experiments highlight the crucial

challenges and barriers for efficient Li-air batteries, such as the high reactivity of the discharge products and electrolyte, precluding, for now, the commercialization of this technology. Aside from the Li$-O_2$ chemistry, this study paves the way to operando NMR analysis of alternative promising metal-O_2 batteries such as Na$-O_2$, Al$-O_2$ or Zn$-O_2$ batteries (which could also benefit from their larger chemical shift and quadrupolar coupling windows), or any electrochemical device involving gas. As such, fuel cells present the common feature to metal-air batteries of providing gas to the cell. The design could be adapted to study fuel cells, providing a continuous flow of fuels and oxidants in the cell. This will represent a significant step towards operando NMR of fuel cells, only scarcely envisioned due to technical difficulties [45,46]. Finally, following the recent advances in in situ MAS NMR [26], the cylindrical design with a close-gas system introduced here could potentially be integrated into a spinning cell for in situ MAS NMR (stop-and-MAS) of Li$-O_2$ cells. This would drastically enhance the spectral resolution and bring additional insights for gaining a complete picture of the chemical and electrochemical mechanisms inside an operating cell. For example, it would offer the possibility of probing the enriched ^{17}O nucleus [19], which has a much larger span of chemical shift and quadrupolar coupling to decipher the different solid-based products in the Li$-O_2$ chemistry.

Declaration of competing interest

The authors declare that they have no known competing financial interests or personal relationships that could have appeared to influence the work reported in this paper.

Acknowledgements

Appendix A. Supplementary data

Supplementary data to this article can be found online at https://doi.org/10.1016/j.ssnmr.2021.101731.

References

[1] A.C. Luntz, B.D. McCloskey, Nonaqueous Li–air batteries: a status report, Chem. Rev. 114 (2014) 11721–11750, https://doi.org/10.1021/cr500054y.

[2] Z. Liang, Q. Zou, Y. Wang, Y.-C. Lu, Recent progress in applying in situ/operando characterization techniques to probe the solid/liquid/gas interfaces of Li–O2 batteries, Small Methods 1 (2017) 1700150, https://doi.org/10.1002/smtd.201700150.

[3] W.-J. Kwak, Rosy, D. Sharon, C. Xia, H. Kim, L.R. Johnson, P.G. Bruce, L.F. Nazar, Y.-K. Sun, A.A. Frimer, M. Noked, S.A. Freunberger, D. Aurbach, Lithium–oxygen batteries and related systems: potential, status, and future, Chem. Rev. 120 (2020) 6626–6683, https://doi.org/10.1021/acs.chemrev.9b00609.

[4] T. Liu, J.P. Vivek, E.W. Zhao, J. Lei, N. Garcia-Araez, C.P. Grey, Current challenges and routes forward for nonaqueous lithium–air batteries, Chem. Rev. 120 (2020) 6558–6625, https://doi.org/10.1021/acs.chemrev.9b00545.

[5] H. Zheng, D. Xiao, X. Li, Y. Liu, Y. Wu, J. Wang, K. Jiang, C. Chen, L. Gu, X. Wei, Y.-S. Hu, Q. Chen, H. Li, New insight in understanding oxygen reduction and evolution in solid-state lithium–oxygen batteries using an in situ environmental scanning electron microscope, Nano Lett. 14 (2014) 4245–4249, https://doi.org/10.1021/nl500862u.

[6] L. Zhong, R.R. Mitchell, Y. Liu, B.M. Gallant, C.V. Thompson, J.Y. Huang, S.X. Mao, Y. Shao-Horn, In situ transmission electron microscopy observations of electrochemical oxidation of Li$_2$O$_2$, Nano Lett. 13 (2013) 2209–2214, https://doi.org/10.1021/nl400731w.

[7] S. Ganapathy, B.D. Adams, G. Stenou, M.S. Anastasaki, K. Goubitz, X.-F. Miao, L.F. Nazar, M. Wagemaker, Nature of Li2O2 oxidation in a Li–O2 battery revealed by operando X-ray diffraction, J. Am. Chem. Soc. (2014), https://doi.org/10.1021/ja508794r.

[8] B. Genorio, J. Staszak-Jirkovský, R.S. Assary, J.G. Connell, D. Strmcnik, C.E. Diesendruck, P.P. Lopes, V.R. Stamenkovic, J.S. Moore, L.A. Curtiss, N.M. Markovic, Superoxide (Electro)Chemistry on well-defined surfaces in organic environments, J. Phys. Chem. C 120 (2016) 15909–15914, https://doi.org/10.1021/acs.jpcc.5b12230.

[9] R. Younesi, M. Hahlin, F. Björefors, P. Johansson, K. Edström, Li–O2 battery degradation by lithium peroxide (Li2O2): a model study, Chem. Mater. 25 (2013) 77–84, https://doi.org/10.1021/cm303226g.

[10] N. Mahne, B. Schafzahl, C. Leypold, M. Leypold, S. Grumm, A. Leitgeb, G.A. Strohmeier, M. Wilkening, O. Fontaine, D. Kramer, C. Slugovc, S.M. Borisov, S.A. Freunberger, Singlet oxygen generation as a major cause for parasitic reactions during cycling of aprotic lithium–oxygen batteries, Nature Energy 2 (2017) 1–9, https://doi.org/10.1038/nenergy.2017.36.

[11] N. Tsiouvaras, S. Meini, I. Buchberger, H.A. Gasteiger, A novel on-line mass spectrometer design for the study of multiple charging cycles of a Li-O2 battery, J. Electrochem. Soc. 160 (2013) A471, https://doi.org/10.1149/2.042303jes.

[12] B.D. McCloskey, A. Valery, A.C. Luntz, S.R. Gowda, G.M. Wallraff, J.M. Garcia, T. Mori, L.E. Krupp, Combining accurate O2 and Li2O2 assays to separate discharge and charge stability limitations in nonaqueous Li–O2 batteries, J. Phys. Chem. Lett. 4 (2013) 2989–2993, https://doi.org/10.1021/jz401659f.

[13] A.C. Luntz, B.D. McCloskey, Li–air batteries: importance of singlet oxygen, Nature Energy 2 (2017) 1–2, https://doi.org/10.1038/nenergy.2017.56.

[14] S.A. Freunberger, Y. Chen, N.E. Drewett, L.J. Hardwick, F. Bardé, P.G. Bruce, The lithium–oxygen battery with ether-based electrolytes, Angew. Chem. Int. Ed. 50 (2011) 8609–8613, https://doi.org/10.1002/anie.201102357.

[15] D. Sharon, V. Etacheri, A. Garsuch, M. Afri, A.A. Frimer, D. Aurbach, On the challenge of electrolyte solutions for Li–air batteries: monitoring oxygen reduction and related reactions in polyether solutions by spectroscopy and EQCM, J. Phys. Chem. Lett. 4 (2013) 127–131, https://doi.org/10.1021/jz3017842.

[16] J. Wandt, P. Jakes, J. Granwehr, H.A. Gasteiger, R.-A. Eichel, Singlet oxygen formation during the charging process of an aprotic lithium–oxygen battery, Angew. Chem. 128 (2016) 7006–7009, https://doi.org/10.1002/ange.201602142.

[17] N. Mahne, S.E. Renfrew, B.D. McCloskey, S.A. Freunberger, Electrochemical oxidation of lithium carbonate generates singlet oxygen, Angew. Chem. Int. Ed. 57 (2018) 5529–5533, https://doi.org/10.1002/anie.201802277.

[18] M. Leskes, A.J. Moore, G.R. Goward, C.P. Grey, Monitoring the electrochemical processes in the lithium–air battery by solid state NMR spectroscopy, J. Phys. Chem. C 117 (2013) 26929–26939, https://doi.org/10.1021/jp410429k.

[19] M. Leskes, N.E. Drewett, L.J. Hardwick, P.G. Bruce, G.R. Goward, C.P. Grey, Direct detection of discharge products in lithium–oxygen batteries by solid-state NMR spectroscopy, Angew. Chem. Int. Ed. 51 (2012) 8560–8563, https://doi.org/10.1002/anie.201202183.

[20] L.A. Huff, J.L. Rapp, L. Zhu, A.A. Gewirth, Identifying lithium–air battery discharge products through 6Li solid-state MAS and 1H–13C solution NMR spectroscopy, J. Power Sources 235 (2013) 87–94, https://doi.org/10.1016/j.jpowsour.2013.01.158.

[21] S. Akabayov Rosy, M. Leskes, M. Noked, Bifunctional role of LiNO3 in Li–O2 batteries: deconvoluting surface and catalytic effects, ACS Appl. Mater. Interfaces 10 (2018) 29622–29629, https://doi.org/10.1021/acsami.8b10054.

[22] T. Liu, M. Leskes, W. Yu, A.J. Moore, L. Zhou, P.M. Bayley, G. Kim, C.P. Grey, Cycling Li-O2 batteries via LiOH formation and decomposition, Science 350 (2015) 530–533, https://doi.org/10.1126/science.aac7730.

[23] T. Liu, G. Kim, E. Jónsson, E. Castillo-Martinez, I. Temprano, Y. Shao, J. Carretero-González, R.N. Kerber, C.P. Grey, Understanding LiOH formation in a Li-O2 battery with LiI and H2O additives, ACS Catal. 9 (2019) 66–77, https://doi.org/10.1021/acscatal.8b02783.

[24] O. Pecher, J. Carretero-González, K.J. Griffith, C.P. Grey, Materials' methods: NMR in battery research, Chem. Mater. 29 (2017) 213–242, https://doi.org/10.1021/acs.chemmater.6b03183.

[25] S.A. Kayser, A. Mester, A. Mertens, P. Jakes, R.-A. Eichel, J. Granwehr, Long-run in operando NMR to investigate the evolution and degradation of battery cells, Phys. Chem. Chem. Phys. 20 (2018) 13765–13776, https://doi.org/10.1039/C8CP01067F.

[26] A.I. Freytag, A.D. Pauric, S.A. Krachkovskiy, G.R. Goward, In situ magic-angle spinning 7Li NMR analysis of a full electrochemical lithium-ion battery using a jelly roll cell design, J. Am. Chem. Soc. 141 (2019) 13758–13761, https://doi.org/10.1021/jacs.9b06885.

[27] J.-P. Zheng, A. Shellikeri, Apparatus for In-Situ NMR Spectroscopy of Metal-Air and Metal-free Air Batteries, 2018, US10126366B2. https://patents.google.com/patent/US10126366B2/en. (Accessed 18 February 2020).

[28] P.J. Rae, E.N. Brown, E.B. Orler, The mechanical properties of poly(ether-ether-ketone) (PEEK) with emphasis on the large compressive strain response, Polymer 48 (2007) 598–615, https://doi.org/10.1016/j.polymer.2006.11.032.

[29] O. Pecher, P.M. Bayley, H. Liu, Z. Liu, N.M. Trease, C.P. Grey, Automatic Tuning Matching Cycler (ATMC) in situ NMR spectroscopy as a novel approach for real-time investigations of Li- and Na-ion batteries, J. Magn. Reson. 265 (2016) 200–209, https://doi.org/10.1016/j.jmr.2016.02.008.

[30] D. Massiot, F. Fayon, M. Capron, I. King, S.L. Calvé, B. Alonso, J.-O. Durand, B. Bujoli, Z. Gan, G. Hoatson, Modelling one- and two-dimensional solid-state NMR spectra, Magn. Reson. Chem. 40 (2002) 70–76, https://doi.org/10.1002/mrc.984.

[31] A.P. Hammersley, FIT2D: a multi-purpose data reduction, analysis and visualization program, J. Appl. Crystallogr. 49 (2016) 646–652, https://doi.org/10.1107/S1600576716000455.

[32] B.D. McCloskey, D.S. Bethune, R.M. Shelby, T. Mori, R. Scheffler, A. Speidel, M. Sherwood, A.C. Luntz, Limitations in rechargeability of Li-O2 batteries and possible origins, J. Phys. Chem. Lett. 3 (2012) 3043–3047, https://doi.org/10.1021/jz301359t.

[33] B.M. Gallant, D.G. Kwabi, R.R. Mitchell, J. Zhou, C.V. Thompson, Y. Shao-Horn, Influence of Li2O2 morphology on oxygen reduction and evolution kinetics in Li–O2 batteries, Energy Environ. Sci. 6 (2013) 2518–2528, https://doi.org/10.1039/C3EE40998H.

[34] M.M. Ottakam Thotiyl, S.A. Freunberger, Z. Peng, P.G. Bruce, The carbon electrode in nonaqueous Li–O2 cells, J. Am. Chem. Soc. 135 (2013) 494–500, https://doi.org/10.1021/ja310258x.

[35] W.-J. Kwak, K.C. Lau, C.-D. Shin, K. Amine, L.A. Curtiss, Y.-K. Sun, A Mo2C/carbon nanotube composite cathode for lithium–oxygen batteries with high energy efficiency and long cycle life, ACS Nano 9 (2015) 4129–4137, https://doi.org/10.1021/acsnano.5b00267.

[36] J.-W. Jung, J.-S. Jang, T.G. Yun, K.R. Yoon, I.-D. Kim, Three-Dimensional nanofibrous air electrode assembled with carbon nanotubes-bridged hollow Fe2O3 nanoparticles for high-performance lithium–oxygen batteries, ACS Appl. Mater. Interfaces 10 (2018) 6531–6540, https://doi.org/10.1021/acsami.7b15421.

[37] L. Carbone, P.T. Moro, M. Gobet, S. Munoz, M. Devany, S.G. Greenbaum, J. Hassoun, Enhanced lithium oxygen battery using a glyme electrolyte and carbon nanotubes, ACS Appl. Mater. Interfaces 10 (2018) 16367–16375, https://doi.org/10.1021/acsami.7b19544.

[38] C.V. Amanchukwu, M. Gauthier, T.P. Batcho, C. Symister, Y. Shao-Horn, J.M. D'Arcy, P.T. Hammond, Evaluation and stability of PEDOT polymer electrodes for Li–O2 batteries, J. Phys. Chem. Lett. 7 (2016) 3770–3775, https://doi.org/10.1021/acs.jpclett.6b01986.

[39] N.B. Aetukuri, B.D. McCloskey, J.M. García, L.E. Krupp, V. Viswanathan, A.C. Luntz, Solvating additives drive solution-mediated electrochemistry and enhance toroid growth in non-aqueous Li–O2 batteries, Nat. Chem. 7 (2015) 50–56, https://doi.org/10.1038/nchem.2132.

[40] H.J. Chang, A.J. Ilott, N.M. Trease, M. Mohammadi, A. Jerschow, C.P. Grey, Correlating microstructural lithium metal growth with electrolyte salt depletion in lithium batteries using 7Li MRI, J. Am. Chem. Soc. 137 (2015) 15209–15216, https://doi.org/10.1021/jacs.5b09385.

[41] R. Bhattacharyya, B. Key, H. Chen, A.S. Best, A.F. Hollenkamp, C.P. Grey, In situ NMR observation of the formation of metallic lithium microstructures in lithium batteries, Nat. Mater. 9 (2010) 504–510, https://doi.org/10.1038/nmat2764.

[42] B.M. Meyer, N. Leifer, S. Sakamoto, S.G. Greenbaum, C.P. Grey, High field multinuclear NMR investigation of the SEI layer in lithium rechargeable batteries, Electrochem. Solid State Lett. 8 (2005) A145–A148, https://doi.org/10.1149/1.1854117.

[43] S.V. Bhat, K. Muthukrishnan, J. Ramakrishna, R. Srinivasan, Lithium nuclear magnetic resonance in lithium formate monohydrate, Phys. Status Solidi A11 (1972) K109, https://doi.org/10.1002/pssa.2210110250.

[44] S.V. Bhat, A.C. Padmanabhan, R. Srinivasan, Lithium nuclear magnetic resonance in lithium acetate dihydrate, Li(CH3COO).2H2O, Acta Crystallogr. B30 (1974) 846–848, https://doi.org/10.1107/S056774087400392X.

[45] O.H. Han, K.S. Han, C.W. Shin, J. Lee, S.-S. Kim, M.S. Um, H.-I. Joh, S.-K. Kim, H.Y. Ha, Observation of methanol behavior in fuel cells in situ by NMR spectroscopy, Angew. Chem. Int. Ed. 51 (2012) 3842–3845, https://doi.org/10.1002/anie.201108330.

[46] A.S. Cattaneo, D.C. Villa, S. Angioni, C. Ferrara, R. Melzi, E. Quartarone, P. Mustarelli, Operando electrochemical NMR microscopy of polymer fuel cells, Energy Environ. Sci. 8 (2015) 2383–2388, https://doi.org/10.1039/C5EE01668A.

Operando NMR Characterization of a Metal-Air Battery using a double-compartment cell design

Magali Gauthier,[a,] Minh Hoang Nguyen,[a,b] Lucie Blondeau,[a] Eddy Foy,[a] Alan Wong,[a,*]*

a) Université Paris-Saclay, CEA, CNRS, NIMBE, 91191, Gif-sur-Yvette, France
b) Current address: Institut de Science des Matériaux de Mulhouse IS2M – UMR CNRS 7361 – UHA, 15, rue Jean Starcky, 68057 Mulhouse CEDEX, France

Corresponding authors: magali.gauthier@cea.fr (MG); alan.wong@cea.fr (AW)
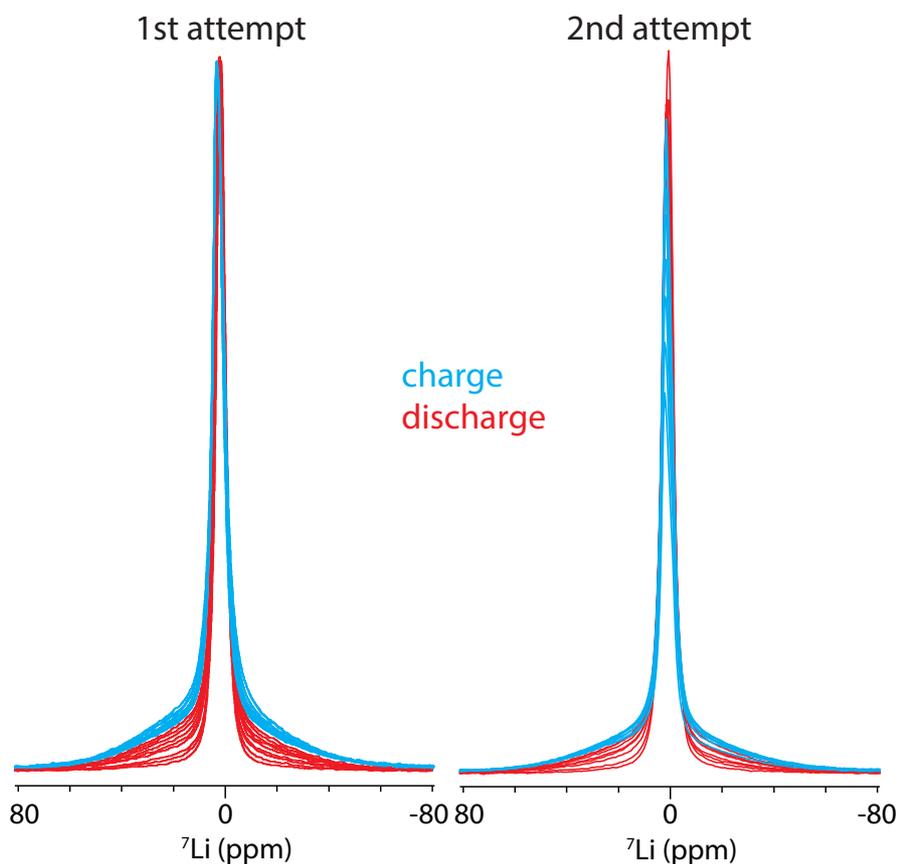
Figure S1. Spectral results of two independent operando ^{7}Li NMR measurements with two individual Li-O$_2$ cells of the same components: CNTs in 1m LiTFSI in DME. *Operando* spectra of the first complete cycle are shown. The similar spectral evolution of the broad resonance illustrate the reproducibility potential with the double-compartment cell.
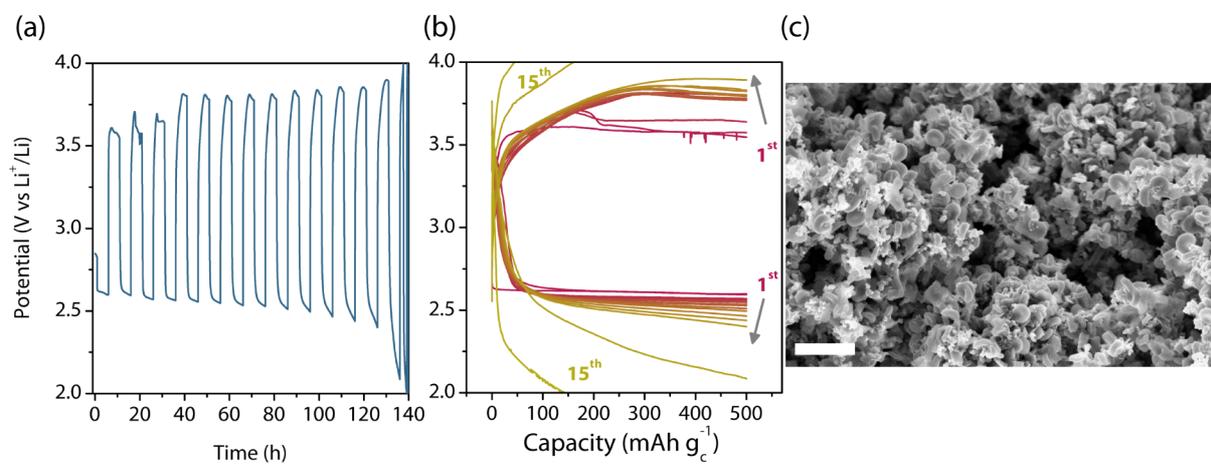
Figure S2. Evolution of the potential as function of (a) time and (b) capacity of a Li-O$_2$ cell with a carbon black electrode cycled at 100 mA g$_c^{-1}$ with a capacity limited to 500 mAh g$_c^{-1}$ in 1M LiTFSI in DME. (c) SEM image of a carbon black electrode discharged up to 500 mAh g$_c^{-1}$ at 100 mA g$_c^{-1}$ in 1M LiTFSI in DME. Scale bar 1 μm.
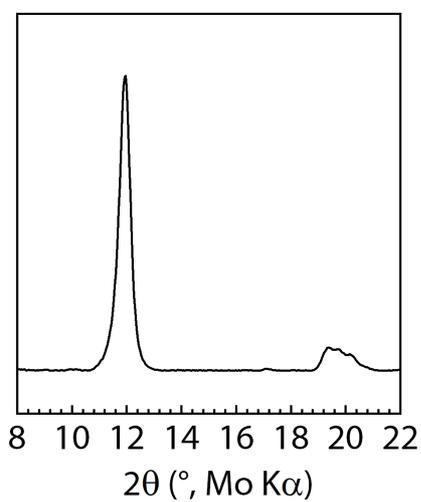

Figure S3. XRD pattern of the pristine CNT electrode.
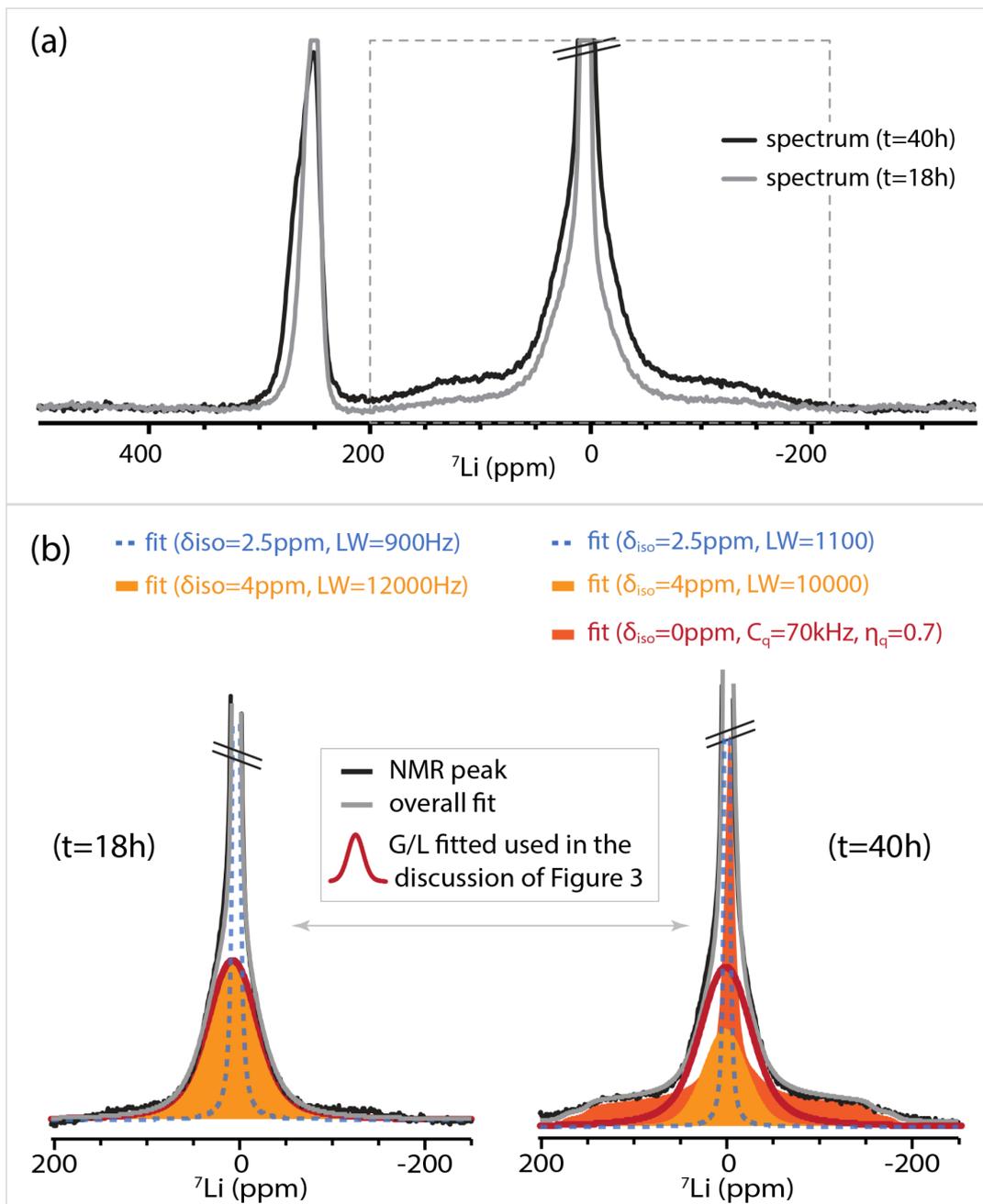
Figure S4. (a) ^{7}Li line shape comparison between the spectrum of t = 18 (end of D1) and 40 h (end of C1). The satellite transition signals of the broad resonance (at 4 ppm; Li$^+$-solids) are evident at t = 40 h, but not at t = 18 h. (b) The broad resonance at 4 ppm was fitted with a single Gaussian/Lorentzian (G/L) line for t = 18 h; whilst a combination of G/L and quadrupolar lines was used for t = 40 h. The fitting was carried out with Topspin.

Based on figure S4, it is evident that at 40 h (end of first charge), the broad resonance can be deconvoluted with two individual lines. The quadrupolar line with satellite transitions could be ascribed to the Li$^+$-solid species with significant C_Q. This could include Li$_2$CO$_3$ [1] and organic compounds such as Li acetate [2] and formate [3]. On the other hand, the G/L line could correspond to Li$_2$O$_2$ [1].

The red G/L line corresponds to the fit of the broad resonance at 4 ppm shown in Figure 3 and its discussion in the manuscript. Note that for t = 40 h, the G/L fit (red line) accounts for both

Li$^+$ species with insignificant C_Q (i.e. Li$_2$O$_2$, etc...) and significant C_Q (i.e. Li$_2$CO$_3$, Li$^+$-organic compounds...).

Indeed, one could carry out the same deconvolution shown in (b) for the entire *operando* data to offer an in-depth deduction of the different Li$^+$ solid species and electrolyte hidden in the broad resonance.
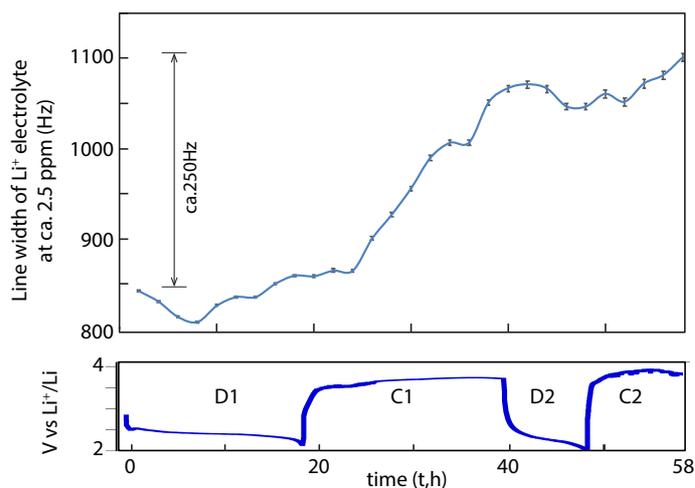
Figure S5. A plot of the line width evolution of the sharp resonance at ~2 ppm (Li$^+$ electrolyte). The line widths were deconvoluted by DMFit.

Reference:

[1] M. Leskes, N. E. Drewett, L. J. Hardwick, P. G. Bruce, G. R. Goward, C. P. Grey, *Angew. Chem. Int. Ed.* 51, 34 (2012): 8560-63.

[2] S.V. Bhat, A.C. Padmanabhan, R. Srinivasan, Lithium Nuclear Magnetic Resonance in Lithium Acetate Dihydrate, Li(CH$_3$COO).2H$_2$O, *Acta Cryst.* B30 (1974): 846–848.

[3] S.V. Bhat, K. Muthukrishnan, J. Ramakrishna, R. Srinivasan, Lithium Nuclear Magnetic Resonance in Lithium Formate Monohydrate, *Phys. Stat. Sol.* A11 (1972): K109.